International Journal of Mechanical Sciences 259 (2023) 108593

Contents lists available at ScienceDirect

International Journal of Mechanical Sciences

journal homepage: www.elsevier.com/locate/ijmecsci

Temperature controlled quasi-zero-stiffness metamaterial beam for broad-range low-frequency band tuning

Zeyi Li [a,b], Kai Wang [a,b,*], Tingting Chen [a], Li Cheng [b], Daolin Xu [a], Jiaxi Zhou [a,*]

[a] College of Mechanical and Vehicle Engineering, Hunan University, Changsha 410082, China
[b] Department of Mechanical Engineering, Hong Kong Polytechnic University, Hong Kong, China

ARTICLE INFO

Keywords:
Metamaterials
Band gap tunability
Quasi-zero stiffness
Shape memory alloys
Low frequency

ABSTRACT

Despite their engineering significance, locally resonant metamaterials are facing the challenge to cope with the need for broad-range band gap adjustment at low-frequencies. To tackle this problem, this study proposes using shape memory alloys (SMAs) to achieve temperature-controlled quasi-zero-stiffness (TC-QZS) metamaterial beam, which entails tunable and low-frequency band gap through ambient temperature changes. The basic configuration of the proposed TC-QZS resonator embraces a negative mechanism, steming from an SMA and a nonlinear geometrical structure. The stiffness of the positive stiffness mechanism can be effectively neutralised by the negative one, and the neutralisation can be adjusted based on temperature change applied to the SMA. The resultant stiffness variation yields broad-range tunability of the resonant frequency of the TC-QZS resonator. The band gap structure of the metamaterial beam is obtained using the transfer matrix method and verified by numerical simulation. Effects of dominant parameters on band gaps are scrutinized. Results show that the frequency range of the band gap can be continuously tuned from 26 to 69 Hz. This study provides guidance for the realisation of band gap tunibility over a wide frequnecy range and lays the groundwork for the development of elastic wave manipulation and vibration isolation.

1. Introduction

Metamaterials are artificially constructed materials or structures that can entail properties or functions which are absent in natural materials [1]. When interacting with a metamaterial structure (scattering, anti-resonance,etc.), wave propagation can be inhibited within certain frequency ranges, referred to as the band gaps [2]. In general, there are two basic mechanisms for the formation mechanism of the elastic wave band gap: bragg scattering and local resonance. The frequency of the Bragg scattering band gap depends on the lattice constant and material parameters [3,4], thereby making it difficult to conciliate between low-frequency band gaps and small-scale structures [5]. On the contrary, the resonant frequency of resonators is the sole determinant of the locally resonant band gaps [3], which is an intrinsic property that depends only on the inertia and stiffness characteristics [6–8]. Therefore, the locally resonant band gap mechanism provides an opportunity for opening the low-frequency band gap through small-scale metamaterials with reasonable load-bearing capability [9,10].

Liu *et al.* [9] first proposed the concept of locally resonant metamaterials in 2000. Low natural frequency is the core of local resonator design. Spring-mass local resonance, which consists of linear springs and mass blocks, is the simplest and the primitive configuration for creating a locally resonant metamaterial [11–13]. It was found that the dynamic response amplitude of the local resonators increase, whereas the propagation of the elastic wave along the main structure decreases when the frequency of the elastic wave is close to the natural frequency of the local resonators [14]. However, two competing elements, namely load-bearing capacity and low stiffness, always exist irrespective of whether it is a traditional spring-mass, or a compact local resonator composed of elastic materials or structures and mass blocks. Therefore, it is difficult for a locally resonant metamaterial composed of conventional elastic elements and mass blocks to open an elastic wave band gap in the low-frequency range, particularly in the ultra-low frequency range [15].

In 2016, Hao et al. [16] proposed a quasi-zero-stiffness (QZS) smooth and discontinuous oscillator and revealed the complex dynamic phenomena of this system through local and global bifurcation analyses. That primitive configuration of the negative-stiffness mechanism consists of two inclined springs [17–27]. The stiffness of the resonator was neutralised by a negative-stiffness mechanism, which results in a

* Corresponding authors.
E-mail addresses: wangkai@hnu.edu.cn (K. Wang), jxizhou@hnu.edu.cn (J. Zhou).

https://doi.org/10.1016/j.ijmecsci.2023.108593
Received 28 March 2023; Received in revised form 11 June 2023; Accepted 1 July 2023
Available online 2 July 2023

decrease in the resonant frequency of the resonator and a low-frequency band gap. It is worth noting that the negative-stiffness mechanism is the core part of the QZS resonator which determines its apparent size and mechanical properties. To date, X-mechanism [28], L-shaped mechanism [29], semicircle-semicircle mechanism [30], cam-roller mechanism [31–33], lever-type [34], and permanent magnetic mechanism [35–37] have been used to achieve negative stiffness and devise QZS resonators. Nevertheless, problems such as size, self-weight, and friction caused by the parallel connection of positive and negative stiffness, limit the application of the aforementioned negative-stiffness structures. To mitigate the deficiencies of mechanical QZS local resonators, structured QZS local resonators have also been designed, offering new opportunities to open low-frequency bandgaps through metamaterials [38–42].

It is not easy to tune the mechanical features of the structured QZS local resonatores owing to the fixed configuration, such hindering the application potential of metamaterials. Consequently, it is necessary to develop active/semi-active low-frequency band gap adjustment methods. Conventionally, changing either the inertia [43–45] or stiffness [40,46–48] of a resonator is the main avenue for regulating the resonant frequency of the resonator to achieve the band gap tuning. Thus far, electronic-controlled [49–59], pneumatic-controlled [60,61] and temperature-controlled [62–71] active/semi-active metamaterials have been attempted to this end. The band gap frequency of electronic-controlled metamaterials, however, offers a small tunable range, whereas pneumatically controlled metamaterials generally require a large volume change to achieve sufficient stiffness changes. Consequently, the practical application potential of existing active/semi-active metamaterials remains limited.

In terms of temperature-controlled metamaterials, the shape memory alloy (SMA) is the main actuator that can yield band gap tuning. The basic principle of the band gap tuning stems from the variation in the elastic modulus engendered by the change in the microstructure of the SMA [62–64]. Owing to the broad-range change in the elastic modulus, metamaterials composed of SMAs offer the potential to regulate the band gap within a large frequency region [65–69]. However, for the single SMA resonators, the dilemma between the low resonant frequency and the stability of the resonator structure remains. Specifically, the individual SMA is not the optimum choice for constructing the resonator to open a low-frequency band gap and achieve band gap tuning in the low-frequency region. Therefore, innovative resonator design based on SMAs is still a promising yet not well mastered research topic.

In this study, an SMA is utilised to conceive a temperature-controlled quasi-zero-stiffness (TC-QZS) resonator. The SMA, combined with a roller-semicircle outline, forms a tunable negative-stiffness mechanism and offers the capacity to neutralise the stiffness of the resonator. The wide-range and temperature-controlled change of the elastic modulus of the SMA would allow for a significant tuning of the stiffness of the resonator. A metamaterial beam with appreciable band tuning cabability is then constructed by periodically mounting the proposed TC-QZS resonators onto a thin beam. The static analysis of the TC-QZS resonator is conducted first, followed by a in-depth discussion on the temperature effect on the elastic modulus of the SMA. The band structure of the TC-QZS metamaterial is examnined by the matrix transfer method and verified in comparison with the wave propagation features extracted from the numerical model. By adjusting the ambient temperature, the band gap can be continuously adjusted over a wide range.

The remainder of this study is organised as follows. In the second Section, the basic structure of the TC-QZS resonator and the principle of the SMA phase transition are described and statically analysed. In Section 3, a dynamic analysis of the TC-QZS metamaterial beam is carried out, including the derivation of the dispersion relation by the transfer matrix method and the numerical simulation using Galerkin method. In Section 4, the effects of the lattice constant, damping ratio, resonator size and material properties of the SMAs on the band gap structure are elucidated. Finally, conclusions are summarised in Section 5.

2. Configuration and design principle

The core of this study is how to design a novel structure to open a band gap in the low frequency range and realise the broad range tunability of the band gap. In this section, a detailed description of the basic configuration of the proposed TC-QZS resonator is first presented and followed by a static analysis. For the completeness of the study and benefit of the readership, the fundamental principle of the elastic modulus variation of the SMA is also presented.

2.1. Principle and configuration

The conceptual design of the proposed TC-QZS metamaterial beam is shown in Fig. 1(a) and the corresponding computational model is shown in Fig. 1(b). The detailed configuration of the TC-QZS resonator is illustrated in Fig. 1(c). The TC-ZQS resonator consists of two vertical springs with a mass block in the middle and two SMA beams on its sides. A linear bearing, completely embedded into the block, is mounted on the guide-bar to ensure the sole motion of the mass block along the vertical direction while reducing the effect of the frictional damping. Additionally, the mass block has a semi-circular outline on its left and right side. Each roller is fixed on the left and right SMA beams, and the distance between the roller and the beam is ignored. One end of the SMA beam is hinged on the frame of the resonator and the other end on a slider installed in a slot. The slider mounted on the slot limits the motion of the SMA beam end to the vertical direction. When the semi-circular outline and roller touch each other, the SMA beam provides a thrust force to the semi-circular outline because of the mid-span deflection. The semi-circular outline of the mass block, SMA beam and roller form a negative-stiffness mechanism, whose restoring force is in the same direction as the deformation of the mass block [72]. This negative-stiffness mechanism is used to assist the deformation of the mass block and neutralise the linear stiffness of the spring. The stiffness of the TC-QZS resonator can be regulated by changing the degree of involvement of the negative-stiffness mechanism, leading to a foreseeable variation in the band frequency of the metamaterial. When the temperature applied to the SMA changes, the elastic modulus of the SMA also changes, resulting in a variation in the degree of neutralisation and tunability of the band frequency of the metamaterial.

As shown in Fig. 1(a), the TC-QZS metamaterial beam comprises a substrate beam and a series of TC-QZS resonators. The resonators are periodically mounted on the substrate beam through a screw thread. The effect of the holes (for the connection of the resonators) in the substrate beam on the metamaterial is not considered here. The main parameters of the metamaterial beam are delineated in Fig. 1(a), including the lattice constant l_c and total length of the beam L. The distance between the ith resonator and the left-hand end of the substrate beam is x_i, which follows $x_i = il_c$.

2.2. Static analysis of the resonator

The anticipated negative-stiffness mechanism is the key component of the TC-QZS metamaterial for achieving low-frequency band gap. It consists of an SMA flexible beam and a pair of roller and semi-circular outlines. Fig. 2 shows the force analysis diagram of the TC-QZS resonator. The radii of the semi-circular outline and the roller are r_1 and r_2, respectively. When the resonator is at the free state, as illustrated in Fig. 2(a), the roller and semi-circular outline do not touch each other so that the SMA beam is in its natural state without compression. The distance between the centre of the roller and the SMA beam is d at this state; SMA beam does not deform when d is greater than r_1+r_2. Under such a scenario, the negative stiffness mechanism consisting of the semi-circular outline and roller fails to neutralise the stiffness of the vertical spring. Consequently, the d should obey $\max\{r_1,r_2\} \le d < r_1 + r_2$.

As shown in Fig. 2(b), the line between the centres of the roller and semi-circular outline is perpendicular to the axis of the spring when the

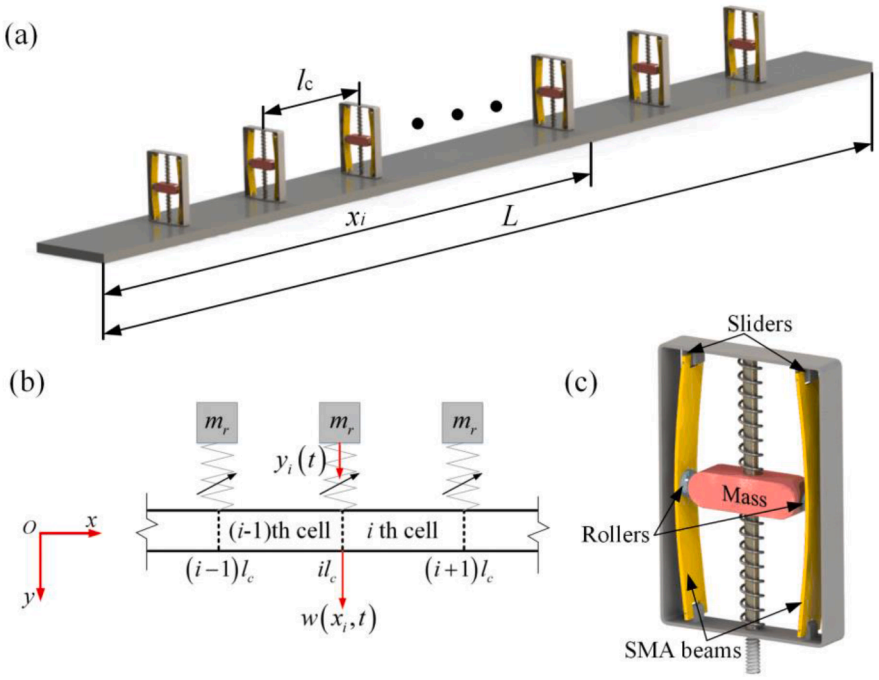

Fig. 1. (a) Conceptual design of the TC-QZS metamaterial beam. (b) Computational model of the metamaterial beam with an infinite length. (c) Configuration of the proposed resonator, mainly consisting of two vertical springs with a mass block and two SMA beams.

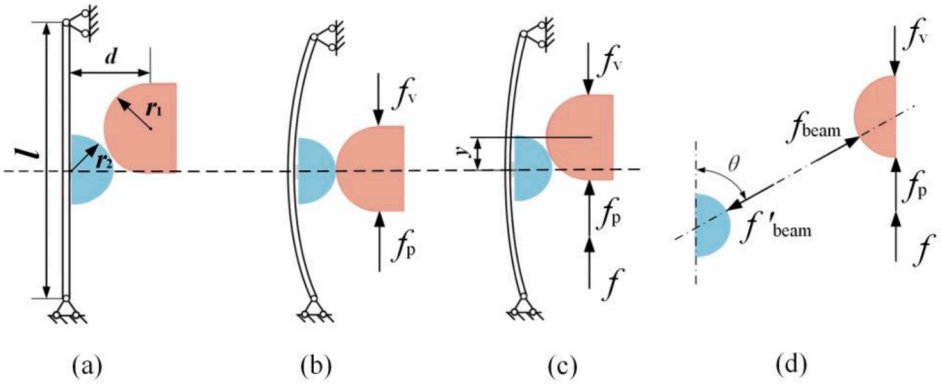

Fig. 2. Schematic of the static analysis of the resonator. (a) Geometric dimensions of the resonator in the free state. (b)The static equilibrium position, where the centre of the roller and semi-circular outline are in the same horizontal line. (c) Compression of the resonator after external excitation f. (d) Force analysis diagram of resonator.

resonator is subjected to a payloadf_p. At this position, the SMA beam exhibits maximum mid-span deflection

$$\Delta_{max} = r_1 + r_2 - d. \tag{1}$$

When an excitation force f acts on the resonator, the semi-circular outline moves in the vertical direction with a distance of y. According to the geometrical relationship shown in Fig. 2(c), the mid-span deflection of the SMA beam can be expressed as

$$\Delta = \sqrt{(r_1 + r_2)^2 - y^2} - d. \tag{2}$$

As the deflection of the SMA beam is not fully released, the SMA beam generates a thrust force on the semi-circular outline through the roller, as shown in Fig. 2(d). The mechanical equilibrium of the roller in the vertical direction can then be written as

$$f + f_p + 2f_{beam}\sin\theta - f_v = 0, \tag{3}$$

where f is the excitation force; f_p and f_v the preload and restoring force provided by the vertical spring, respectively; and f_{beam} denotes the thrust force (as a result of the deflection of the SMA beam) working on the semi-circular outline, which writes

$$f_{beam} = \frac{48E(T)I}{l^3}\frac{(r_1 + r_2)\Delta}{\sqrt{(r_1 + r_2)^2 - y^2}}, \tag{4}$$

where $E(T)I$ denotes the flexural rigidity expressed as the product of elastic model of the SMA $E(T)$ which is a function of temperature (T), and the area moment of inertia of the SMA beam I. l is the length of the flexible beam.

When the mass block moves away from the equilibrium position, its maximum relative displacement, corresponding to the scenario in which the mid-span deflection of the SMA beam is completely released, can be written as

$$y_{max} = \sqrt{(r_1 + r_2)^2 - d^2}. \tag{5}$$

Under these circumstances, the negative-stiffness mechanism within the TC-QZS resonator is not deployed, so that the resonator stiffness is equal to that of the linear vertical springs. Considering the hypothesis of small-amplitude oscillations, the semi-circular outline and roller always remain in contact. Therefore, the relative displacement of the TC-QZS resonator during normal operation should satisfy

$$y \in [-y_{\max}, y_{\max}]. \tag{6}$$

Substituting Eq. (4) into Eq. (3) yields the restoring force as a function of the displacement as

$$f(y,T) = 2k_v y - \frac{96E(T)I}{l^3}\left(1 - \frac{d}{\sqrt{(r_1+r_2)^2 - y^2}}\right)y. \tag{7}$$

By differentiating the expression of the restoring force with respect to the relative displacement y, the nonlinear expression of the stiffness of the TC-QZS resonator can be obtained as

$$k(y,T) = 2k_v - \frac{96E(T)I}{l^3}\left\{1 - \frac{d(r_1+r_2)^2}{\left[(r_1+r_2)^2 - y^2\right]^{\frac{3}{2}}}\right\}. \tag{8}$$

The stiffness of the TC-QZS resonator is affected by the temperature through temperature-dependant elastic modulus.

After introducing a parameter γ to evaluate the degree of neutralisation of the negative stiffness, the stiffness of the TC-QZS resonator can be re-expressed as

$$k(y,T) = 2\gamma k_v + 2(1-\gamma)k_v - \frac{96E(T)I}{l^3}\left\{1 - \frac{d(r_1+r_2)^2}{\left[(r_1+r_2)^2 - y^2\right]^{\frac{3}{2}}}\right\}, \tag{9}$$

γ is the ratio of the remaining stiffness of the resonator at the equilibrium position to the stiffness of the vertical springs.

To reduce the stiffness of the TC-QZS resonator at the static equilibrium position ($y = 0$) from $2k_v$ to $2\gamma k_v$, let

$$2(1-\gamma)k_v - \frac{96E(T)I}{l^3}\left\{1 - \frac{d}{r_1+r_2}\right\} = 0. \tag{10}$$

Consequently, to meet the required target band gap position, appropriate parameters of the TC-QZS resonator can be designed according to Eq. (10) by selecting an appropriate value for γ.

2.3. Principle of the stiffness tunability

Since the cornerstone of low frequency band gap tuning is the temperature modulated change in the Young's modulus of the SMA beam, the material properties of the SMA are discussed in this section. To avoid the influence of the pseudo-elastic effect on the metal phase, the stress of the SMA is assumed to be always below the minimum stress for the onset of stress-induced phase transitions [66]. In this case, only the martensite and austenite phases appear at low and high temperatures at the beginning of the phase transition, respectively. Hence, the ascending order of the transformation temperatures of the SMA is as follows: martensite finished temperature (M_f), martensite started (M_s), austenite started (A_s) and austenite finished (A_f). To describe the phase transition mechanism of the SMA under a temperature change, the martensitic fraction ξ was introduced to represent the phase variation of martensite. According to the Brinson's model, the martensite fraction during the cooling process can be represented as follows: [62]

$$\xi_c = \begin{cases} 1, T < M_f \\ \frac{1}{2}\left[\cos\left(\pi\frac{T - M_f}{M_s - M_f}\right) + 1\right], M_f \le T \le M_s \\ 0, T > M_s \end{cases}. \tag{11}$$

Similarly, the martensite fraction during the heating process can be expressed as

$$\xi_h = \begin{cases} 1, & T < A_s \\ \frac{1}{2}\left[\cos\left(\pi\frac{T - A_s}{A_f - A_s}\right) + 1\right], & A_s \le T \le A_f \\ 0, & T > A_f \end{cases}. \tag{12}$$

Based on the martensite fraction defined above, the influence of temperature on the elastic modulus of the SMA can be expressed as

$$E(\xi) = E_A + \xi\cdot(E_M - E_A), \tag{13}$$

where E_M and E_A denote the elastic moduli of the SMA in the fully martensitic and fully austenitic phases, respectively. By substituting Eqs. (11) and (12) into Eq. (13), the relationship between the elastic modulus of the SMA and temperature can be written as follows:

$$E_c(T) = \begin{cases} E_M, T < M_f \\ E_A + \frac{1}{2}\left[\cos\left(\pi\frac{T - M_f}{M_s - M_f}\right) + 1\right]\cdot(E_M - E_A), M_f \le T \le M_s \\ E_A, T > M_s \end{cases},$$

$$E_h(T) = \begin{cases} E_M, & T < A_s \\ E_A + \frac{1}{2}\left[\cos\left(\pi\frac{T - A_s}{A_f - A_s}\right) + 1\right]\cdot(E_M - E_A), & A_s \le T \le A_f \\ E_A, & T > A_f \end{cases}, \tag{14}$$

where subscripts c and h denote the cooling and heating processes, respectively. Based on Eq. (14) and material parameters tabulated in Table 1 [62], the elastic modulus variation with respect to the temperature is shown in Fig. 3, in which the red and blue lines represent the heating and cooling processes, respectively. The arrows indicate the direction of the temperature change. By projecting the 3D curve onto the $\xi - T$ and $E - T$ planes, the relationships between ξ and T as well as E and T can be obtained. As shown by the red dashed and dotted lines, the SMA is in the fully martensitic phase ($\xi_0 = 1$, $E = E_M$) before the heating process. With the increase of temperature, the metallographic structure of the SMA undergoes a phase transition as the temperature reaches A_s. The martensite fraction gradually decreases from 1 and the elastic modulus of the SMA increases from E_M. As the temperature rises to A_f, the martensite fraction of the SMA drops to 0, and its elastic modulus equals E_A. With a continuous increase in temperature, both the martensite fraction and elastic modulus remain unchanged.

The martensitic phase and elastic modulus of the SMA varying with the temperature dropping are elaborated by blue solid and dotted lines in Fig. 3. The inceptive temperature of the SMA is higher than A_f. The SMA begins to transform from the fully austenitic phase ($\xi_0 = 0$, $E = E_A$) to the fully martensitic phase ($\xi = 1$, $E = E_M$) as temperature dropping from M_s to M_f. With the fall of the temperature further, the martensite fraction, the metallic phase and the elastic modulus of the SMA all remain unchanged.

Table 1
Parameters of the SMA.

Parameters	Descriptions	Values
E_M	The martensitic modulus	26.3GPa
E_A	The austenitic modulus	67GPa
μ	Poisson's ratio	0.33
M_f	The martensite finished temperature	9 °C
M_s	The martensite started temperature	18.4 °C
A_s	The austenite started temperature	34.5 °C
A_f	The austenite finished temperature	49 °C
σ_s^M	The minimum stress for the onset of stress-induced phase transitions	100MPa

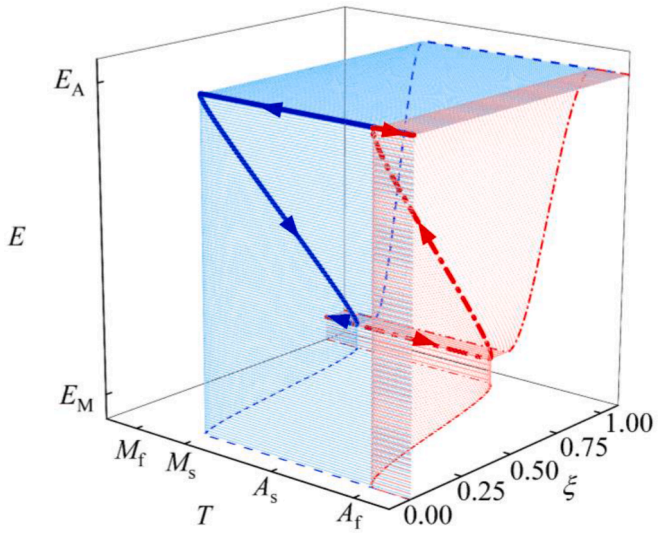

Fig. 3. Evolutions of the martensitic fraction and the SMA elastic modulus for the heating (dot crossed red line) and cooling (solid blue line) processes, respectively. The arrow shows the direction of the temperature change.

2.4. Quantitative analysis of the stiffness of the TC-QZS resonator

After clarifying the fundamental principle of the band gap tunability, the specific stiffness characteristics of the TC-QZS resonator can be obtained through the design of the geometric parameters of the resonator. Assuming that the maximum stress of the flexible SMA beam at the equilibrium position is always less than the onset of the stress-induced phase transition σ_s^M, the elastic modulus of the SMA ranges from E_M to E_A when the temperature changes. To maximise the low-frequency band gap tuning, the elastic modulus E_A is selected as the initial parameter to obtain the parametric condition of low stiffness when $\gamma = 0.085$. Subsequently, the resonator stiffness increases due to the variation in the ambient temperature.

The strength of the SMA beam is checked to verify the reliability of the resonator design. At the equilibrium position, the SMA beam possesses the maximum mid-span deflection and resultant maximum stress, which can be expressed as

$$\sigma_{max} = \frac{M_{max}}{W} = 96.48\text{MPa} < [\sigma], \tag{15}$$

where M_{max} is the bending moment of the SMA beam at maximum deflection and $W = bh^3/6$ is the flexural factor in this section. The allowable stress [σ]is set to the minimum stress for the onset of stress-induced phase transitions, that is, $[\sigma] = \sigma_s^M$. As the maximum stress at the equilibrium position is less than the allowable value, the SMA beam satisfies the strength requirement.

Fig. 4 shows the force and stiffness versus displacement of the positive and negative stiffness mechanisms, as well as the whole resonator. Only the vertical displacement range within which the negative-stiffness mechanism in the TC-QZS resonator takes effect is selected. The black dot-dashed lines denote the restoring force and stiffness provided by the vertical spring, which can be regarded as the positive mechanism. While the dotted lines indicate the restoring force and stiffness provided by the negative-stiffness mechanism (combined by an SMA beam and a roller-semicircular outline). The solid lines with stars represent the restoring force and stiffness of the resonator when the positive stiffness mechanism and the negative stiffness mechanism are in parallel. The blue and red lines indicate the restoring force and stiffness of SMA at low and high temperatures, respectively. It can be seen from the Fig. 4(a) that near the equilibrium position, the restoring forces at both low and high temperatures are influenced by the negative stiffness mechanism and tend to be flat. Moreover, as shown in Fig. 4(b), the negative stiffness mechanism successfully neutralises the positive stiffness and reduces the stiffness of the resonator near the equilibrium position. The TC-QZS resonator achieves quasi-zero stiffness at high temperature, which is the original intention of the design. Therefore, the stiffness of resonator near the equilibrium position at high temperature is closer to zero. The stiffness in each temperature condition is less than the stiffness of the vertical spring within the displacement range shown by the orange shaded area in the figure, which can be regarded as the region where the negative stiffness mechanism takes effect.

Fig. 4 shows the stiffness of the resonator when SMA is in the fully martensitic and fully austenitic phases. However, since the phase transition of SMA is a continuous process with temperature, the relationship between the resonator stiffness and temperature is shown in Fig. 5. The blue and red surfaces represent the cooling and heating processes, respectively. The two grey planes represent the started and finished temperatures of the phase transition, and the middle is the phase transition region. The arrows indicate the direction of temperature change.

The stiffness surfaces of the TC-QZS resonator are symmetrical with respect to the equilibrium position ($y = 0$), regardless of whether the SMA experiences a cooling or heating process. For the cooling process, as shown in Fig. 5(a), the stiffness of the TC-QZS resonator remains unchanged when the temperature is higher than the martensite started temperature. Then, as the temperature falls below the martensite started temperature and above the martensite finished one, the stiffness of the

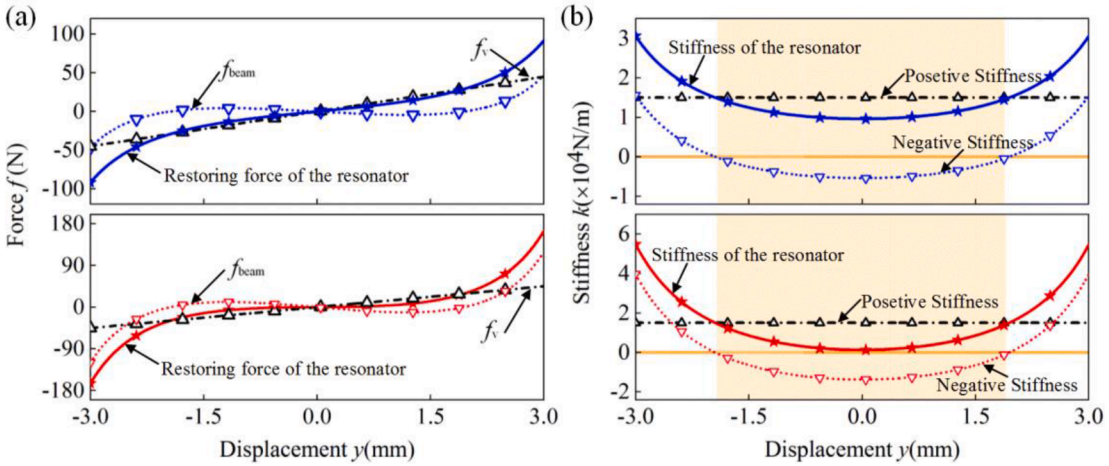

Fig. 4. Static analysis of the TC-QZS resonator. (a) The restoring force versus displacement curves. (b) The stiffness versus displacement curves. The blue and red lines indicate that SMA is in the low temperature martensitic phase and high temperature austenitic one.

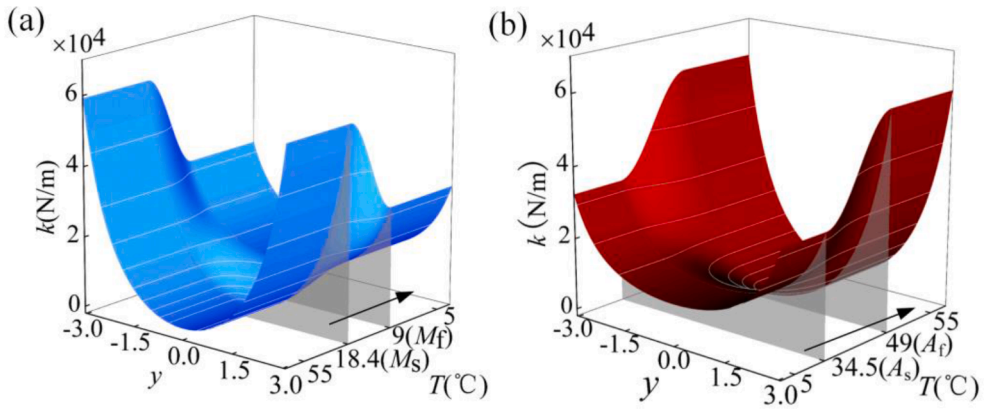

Fig. 5. Variation diagram of the stiffness of the TC-QZS resonators corresponding to the temperature and vertical displacement. The blue and red surfaces stand for the cooling and heating processes, respectively. The arrow shows the direction of the temperature change.

TC-QZS resonator at the equilibrium position increases with a decrease in temperature. At the end, when the temperature is below the martensite finished temperature, the stiffness remains unchanged.

Contrary to the cooling process, the stiffness of the TC-QZS resonator at the equilibrium position first remains stable during heating, then decreases and finally plateaus again. The observed changes in resonator stiffness with temperature can be attributed to the metallic phase transition of the SMA. Specifically, the elastic modulus of the SMA remains unchanged if its temperature is below the martensite finished temperature M_f or above the austenite finished temperature A_f. A larger austenitic modulus (E_A) compared with that of the martensitic modulus (E_M) results in a greater degree of neutralisation of the negative-stiffness mechanism for the positive stiffness, thereby enabling a lower resonator stiffness in the high-temperature region. When the SMA is cooled from A_f to M_f or heated from M_f to A_f, its metallic phase undergoes a phase transition, which in turn influences the stiffness of the resonator.

3. Dynamics of the metamaterial beam

The band structure and wave propagation features along the metamaterial are the two main tools used to evaluate the advantages of the proposed metamaterial. In this section, we first derive the dispersion relation of the TC-QZS metamaterial and subsequently examnine the band structures. Wave propagation along the substrate beam is also carried out by means of the Galerkin's method.

3.1. Dispersion relation

Considering the hypothesis that the TC-QZS metamaterial is of infinite length and that an infinite number of TC-QZS resonators are uniformly mounted on the substrate beam, the equation of motion of the substrate beam writes

$$E_sI_s\frac{\partial^4 w}{\partial x^4}+\rho A_s\frac{\partial^2 w}{\partial t^2}=0, \tag{16}$$

where E_sI_s represents the flexural stiffness expressed as the product of the elastic model E_s and the area moment of inertia I_s; ρ and $A_s$denote the density and cross-sectional area of the substrate beam, respectively; and $w(x, t)$ is the deflection of the substrate beam at position x and time t.

As shown in Fig. 4, the stiffness of the TC-QZS resonator at the equilibrium position is equal to that of the γk_v. If the resonator is out of the equilibrium position with a small displacement, its stiffness approaches that of the equilibrium position. Consequently, the nonlinear stiffness of the TC-QZS resonator can be linearised as γk_v under the scenario that the excitation amplitude applied on it is not large [17]. The nonlinear restoring force of the TC-QZS resonator can be reduced to the product of the relative displacement and stiffness at the equilibrium position, according to the linearized stiffness. Then, the equation of motion of the ith TC-QZS resonator can be expressed as

$$m_r\ddot{y}_i(t)-k(0,T_c)[w(x_i,t)-y_i(t)]=0, \tag{17}$$

where $k(0, T_c)$ denotes the stiffness of the TC-QZS resonator at the equilibrium position under ambient temperature T_c; m_r is the mass of the resonator;$y_i(t) = Y_ie^{\sqrt{-1}\omega t}$is the absolute displacement of the ith resonator and Y_i is the displacement amplitude. Additionally, $w(x_i,t)$stands for the deflection of the substrate beam at the position of x_i and time t.

Assuming that the deflection of the substrate beam can be written as$w(x,t) = W(x)e^{\sqrt{-1}\omega t}$, where $W(x)$ stands for the mode shape function, which is given by

$$W(x)=\boldsymbol{\psi}\Phi(x)^T, \tag{18}$$

where $\boldsymbol{\Phi}(x)=\{\cos(\beta x)\ \ \sin(\beta x)\ \ \cosh(\beta x)\ \ \sinh(\beta x)\}$ and $\beta=\sqrt[4]{\rho A_s\omega^2/E_sI_s}$ is the flexural wavenumber; $\boldsymbol{\psi}=\{A\ \ B\ \ C\ \ D\}$ denotes a matrix of unknown coefficients.

For the ith unit cell, as shown in Fig. 1(b), its local coordinate x' can be expressed by the global coordinate x and lattice constant as follows:

$$x'=x-il_c,\ il_c\le x\le(i+1)l_c. \tag{19}$$

The mode shape function of the ith unit cell can be written as

$$W_i(x')=\boldsymbol{\psi}_i\boldsymbol{\Phi}_i(x')^T. \tag{20}$$

Considering the continuities of the displacement, slope, bending moment and shear force of the substrate beam at the connection point of the ith resonator, one has:

$$\begin{cases} W_{i-1}(l_c)=W_i(0);\\ W'_{i-1}(l_c)=W'_i(0);\\ E_sI_sW''_{i-1}(l_c)=E_sI_sW''_i(0);\\ E_sI_sW'''_{i-1}(l_c)+F_i=E_sI_sW'''_i(0). \end{cases} \tag{21}$$

According to the Floquet-Bloch theorem [17], the coefficient matrix between adjacent cells obeys

$$\boldsymbol{\psi}_i=e^{\sqrt{-1}ql_c}\boldsymbol{\psi}_{i-1}, \tag{22}$$

where q denotes the flexural wave vector. Substitute Eq. (20) into Eq. (21) gives

$$\mathbf{H}\boldsymbol{\psi}_{i-1}=\mathbf{G}\boldsymbol{\psi}_i, \tag{23}$$

where

$$\mathbf{H}=\begin{bmatrix}\cos(\beta l_c) & \sin(\beta l_c) & \cosh(\beta l_c) & \sinh(\beta l_c)\\ -\beta\sin(\beta l_c) & \beta\cos(\beta l_c) & \beta\sinh(\beta l_c) & \beta\cosh(\beta l_c)\\ -\beta^2\cos(\beta l_c) & -\beta^2\sin(\beta l_c) & \beta^2\cosh(\beta l_c) & \beta^2\sinh(\beta l_c)\\ \beta^3\sin(\beta l_c) & -\beta^3\cos(\beta l_c) & \beta^3\sinh(\beta l_c) & \beta^3\cosh(\beta l_c)\end{bmatrix}, \tag{24}$$

$$\mathbf{G}=\begin{bmatrix}1 & 0 & 1 & 0\\ 0 & \beta & 0 & \beta\\ -\beta^2 & 0 & \beta^2 & 0\\ -\frac{1}{EI}\frac{k(0,T_c)m_r\omega^2}{k(0,T_c)-m_r\omega^2} & -\beta^3 & \frac{1}{EI}\frac{k(0,T_c)m_r\omega^2}{k(0,T_c)-m_r\omega^2} & \beta^3\end{bmatrix}. \tag{25}$$

Substituting Eq. (22) into Eq. (23) leads to the dispersion relation of the TC-QZS metamaterial beam as

$$\left|\mathbf{G}^{-1}\mathbf{H}-e^{\sqrt{-1}ql_c}\mathbf{I}\right|=0. \tag{26}$$

For an arbitrary ω, one can obtain the corresponding wave vector q by solving Eq. (26). The band structure of the TC-QZS metamaterial beam can be obtained by determining the relationship between the frequency and the real or the imaginary parts of the complex solution of the wave vector.

Using the parameters tabulated in Table 2, the band structures of the TC-QZS metamaterial beam with SMA in the fully martensitic ($E = 26.3$ GPa) and fully austenitic ($E = 67$ GPa) phases are delineated in Fig. 6(a). The grey shaded areas denote the band gap regions where wave propagation along the metamaterial is prohibited. Obviously, the position, width and depth of the band gap of the TC-QZS metamaterial are significantly different in the case of the fully martensitic and fully austenitic phases. Specifically, when the metamaterial is at a low temperature, that is, the SMA is in the fully martensitic phase, the band gap of the TC-QZS metamaterial appears in the frequency range of 69.5–105.5 Hz. In contrast, at the temperatures higher than A_f, the initial frequency of the band gap (ranging from 25 to 38.5 Hz) is about a quarter of the highest band gap frequency at low temperatures.

To better visualise the band structure changes with temperature, the position and the width of the band gap under continuous temperature change are presented in Fig. 6(b). The upper and lower solid black lines indicate the start and end frequencies of the band gap, respectively. The blue and red shaded areas between the two solid lines indicate the band gap region of the TC-QZS metamaterial under the cooling and heating processes, respectively. In the scenario where the SMA experiences a cooling process, the band gap frequency remains unchanged if the SMA temperature is above M_s. When the SMA temperature is in the range of M_f to M_s, the band gap frequency shifts from a low frequency range to a high one with a decrease in temperature. If the SMA temperature falls further and is below M_f, the band gap frequency remains constant. Contrary to the cooling process, when the SMA is heated, the band gap frequency remains unchanged firstly, then decreases from a high frequency range to a low value and remains unchanged again with the increase in SMA temperature. The variation in the band gap frequency with the SMA temperature is in line with that of the TC-QZS resonator stiffness with the SMA temperature. It suggests that the variation in the resonator stiffness is the intrinsic cause of the temperature effect on the band gap frequency.

Table 2
Parameters of the TC-QZS metamaterial beam.

Parameters	Descriptions	Values
E_s(GPa)	Elastic modulus of the substrate beam	70
I_s(m^4)	Area moment of inertia of the substrate beam	7.0312×10^{-12}
ρ(kg/m^3)	Density of the substrate beam	2600
μ	Poisson's ratio of the substrate beam	0.3
A_s(m^2)	Area of the substrate beam	1.5×10^{-4}
L(m)	Length of the substrate beam	1
l_c(m)	Lattice constant of the metamaterial beam	0.1
I(m^4)	Area moment of inertia of the SMA flexible beam	8×10^{-12}
l(m)	Length of the SMA flexible beam	0.1
k_v(N/m)	Stiffness of vertical spring	7.5×10^3
m_r(kg)	Mass of resonator	0.05
r_1(m)	Radius of the semi-circular outline	0.003
r_2(m)	Radius of the roller	0.0015
d(m)	Distance between the centre of the semi-circular outline and the flexible beam	0.0033
ζ_m(Ns/m)	Modal damping	0.02
ζ_0(Ns/m)	Damping of resonators	0.01

3.2. Numerical simulation

To verify the theoretical band structures, the wave propagation along the TC-QZS-metamaterial with a finite length L is analysed in this section based on the Galerkin method. Considering a harmonic excitation imposed on the left-hand end of the substrate beam, the equation of motion of the substrate beam can be expressed as

$$E_sI_s\frac{\partial^4w(x,t)}{\partial x^4}+\rho A_s\frac{\partial^2w(x,t)}{\partial t^2}=f_E(t)\delta(x-0)+F_{ADD}(x,t)\delta(x-x_c), \tag{27}$$

where $f_E(t)$ is the excitation, $F_{ADD}(x,t)$ denotes the restoring force provided by the TC-QZS resonator, x_c is the distance from the left-hand end of the substrate beam to the point of action of the resonator and $\delta(x)$ is the Dirac delta function utilised to represent the point of action and can be expressed as

$$\int_{-\infty}^{+\infty}\delta(x)\mathrm{d}x=1. \tag{28}$$

With surface-mounted TC-QZS resonators, the force provided by each resonator is given by

$$F_{ADD}(x,t)=2k_vy_{rel}(x,t)-\frac{96E(T)Iy_{rel}(x,t)}{L^3}\left[1-\frac{b}{\sqrt{(r_1+r_2)^2-y(x,t)_{rel}^2}}\right], \tag{29}$$

where $y_{rel}(x,t)=y(t)-w(x,t)$ is the relative displacement between the TC-QZS resonator and substrate beam.

According to the Galerkin method, the transverse displacement of the substrate beam can be discretised as follows:

$$w(x,t)=\sum_{m=1}^{M}\phi_m(x)\eta_m(t), \tag{30}$$

where $\phi_m(x)$ is the trial function and $\eta_m(t)$denotes the modal coordinate of the beam for the mth mode. Variable M represents the number of Galerkin truncations whose value should be sufficiently large to satisfy the requirement of computational accuracy.

By substituting Eq. (30) into Eq. (27), the equation of motion of the substrate beam can be rewritten as:

$$E_sI_s\sum_{m=1}^{M}\eta_m(t)\frac{\mathrm{d}^4\phi_m(x)}{\mathrm{d}x^4}+\rho A_s\sum_{m=1}^{M}\phi_m(x)\frac{\mathrm{d}^2\eta_m(t)}{\mathrm{d}t^2}=f_E(t)\delta(x-0)+\sum_{j=1}^{n}F_{ADD}(x_j,t)\delta(x-x_j), \tag{31}$$

where n is the total number of TC-QZS resonators assembled on the substrate beam. Multiplying Eq. (31) by the weight function $\varphi_m(x)$ and integrating it from 0 to L, Eq. (31) can be rewritten as follows:

$$\begin{aligned}&E_SI_S\sum_{m=1}^{M}\int_0^L\phi_m^{(4)}(x)\varphi_m(x)dx\cdot\eta_m(t)+\rho A_S\sum_{m=1}^{M}\int_0^L\phi_m(x)\varphi_m(x)dx\cdot\ddot{\eta}_m(t)\\&=\int_0^L\varphi_m(x)\delta(x-0)dx\cdot f_E(t)+\sum_{j=1}^{n}\int_0^L\varphi_m(x)F_{ADD}(x_j,t)\delta(x-x_j)dz.\end{aligned} \tag{32}$$

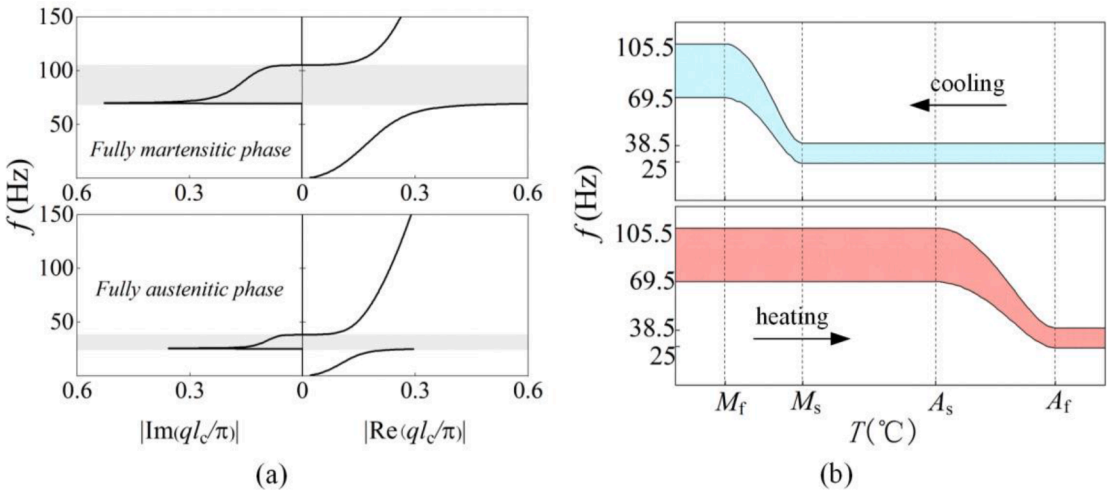

Fig. 6. (a) Theoretical band structures of the TC-QZS metamaterial when the metallographic phase of the SMA is at fully martensitic and fully austenitic phases respectively. The grey shaded area indicates the band gap. (b) Variation of the band structure with temperature change. The blue and red shaded areas represent the band gap regions during the cooling and heating processes, respectively, and the arrows indicate the direction of the temperature change.

Note that both the weight function and the trial function in the work are selected as the mode functions of the Euler-Bernoulli beam. The boundary conditions were assumed to be free at both ends; that is, there were no limitations applied to both ends, and the beam could vibrate freely. The mode functions of the Euler-Bernoulli beam with free-free boundary condition can be given by [17]

$$\phi_m(x) = \varphi_m(x) = \sin(\beta_m x) + \sinh(\beta_m x) + \frac{\sin(\beta_m l) - \sinh(\beta_m l)}{\cosh(\beta_m l) - \cos(\beta_m l)}[\cos(\beta_m x) + \cosh(\beta_m x)], \tag{33}$$

where β denotes the wave number which can be determined from the frequency equation

$$\cos(\beta_m l)\cosh(\beta_m l) = 1. \tag{34}$$

Considering the orthogonality of the mode functions and introducing the modal damping and damping of resonators, Eq. (32) can be rewritten as follows:

$$m_m\ddot{\eta}_m + c_m\dot{\eta}_m + k_m\eta = \phi_m(0)f_E + \sum_{j=1}^{n}\phi_m(x_j)F_{ADD} + \sum_{j=1}^{n}\phi_m(x_j)f_d(x_j,t), \tag{35}$$

where

$$\begin{aligned} m_m &= \rho A\int_0^l \phi_m^2(x)dz, \\ k_m &= EI\int_0^l \phi_m^{(4)}(x)\phi(x)dz, \\ c_m &= 2\zeta_m\sqrt{m_m k_m}, \\ f_d(x_j,t) &= 2\zeta_0\sqrt{m_r k_v}\left[\dot{y}_j(t) - \sum_{m=1}^{M}\phi_m(x_j)\dot{\eta}_m(t)\right], \end{aligned} \tag{36}$$

where $f_d(x_j,t)$ is the internal damping force of the jth resonator; ζ_m and ζ_0 are the damping ratios of the mth beam mode and resonator, respectively, which are introduced to damp the free vibrations. In the calculation process, $\zeta_m = 0.02$ and $\zeta_0 = 0.01$ were taken respectively.

Additionally, the equation of motion of the jth resonator is given by

$$m_r\ddot{y}_j(t) + f_d(x_j,t) + F_{ADD}(x_j,t) = 0, \tag{37}$$

By solving Eqs. (35) and (37), the displacements in the generalised coordinates and the absolute displacements of all resonators were obtained directly. The accurate deflection response of the substrate beam can then be obtained by substituting the generalised displacements into Eq. (30). The wave transmittance, defined as the ratio of the displacement response of the substrate beam at both ends of the metamaterial, and the wave suppression capacity of the metamaterial can be elaborated in detail. When the frequency is located in the band gap range, the wave transmittance value is less than zero dB and the corresponding wave is attenuated because of the effect of the local resonance of the resonator. In contrast, when the frequency is outside the band gap, the wave transmittance is greater than zero, and the wave propagation along the metamaterial is enlarged.

However, special conditions are applied if the wave frequency is in the ultralow frequency range (about 0 Hz to 30 Hz). Although the wave transmittance curve is completely below zero, this frequency range cannot be considered as the band gap region. Such a false image is ascribed to the eccentric rotation of the rigid body of the substrate beam at lower the excitation frequencies. Because the centre of rotation of the substrate beam is close to the right-hand end, the rigid displacement of the substrate beam at the left-hand end is greater than that at the right-hand end, resulting in a transmittance less than zero in the ultralow frequency range. Under these circumstances, the band gap area predicted by the wave transmittance can be determined by selecting the frequency range where the wave transmittance is less than that when the frequency is close to zero Hz (0.01 Hz herein). With an increase in frequency, the effect of the rigid rotation displacement of the substrate beam on the wave transmittance gradually decreases. Namely, in terms of the frequency range in the relatively high-frequency region, the excitation frequency can be considered to belong to a band gap region if the corresponding wave transmittance is less than zero dB.

Fig. 7 shows the wave transmittance of the TC-QZS metamaterial beam when the SMA is in the fully austenitic (red solid line with circle) and fully martensitic (blue solid line with square) phases. According to the selection criteria stated above, the band gap ranges predicted by the wave transmittance are marked by the red and blue shaded areas. The band gap of the TC-QZS metamaterial ranges from 65 Hz to 98.5 Hz when the SMA is in the low-temperature martensitic phase. As the SMA temperature increases above the austenite finished temperature A_f, the SMA is in the high-temperature austenitic phase and the elastic modulus of the SMA increases significantly. Then, the stiffness of the TC-QZS resonator at the equilibrium position decreases because of the greater degree of neutralisation of the positional stiffness of the resonator, resulting in lower band gap (about 25.2 Hz to 48.8 Hz) compared with that when the SMA is in the low-temperature martensitic phase. Conversely, in the cooling process, the band gap frequency of the TC-

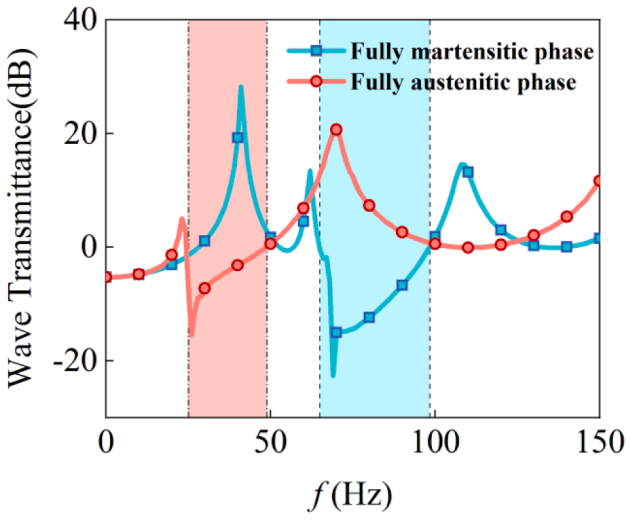

Fig. 7. Wave transmittance along the TC-QZS metamaterial under two special scenarios where the SMA is in fully austenitic phase (solid line with circles in red) and fully martensitic phase (solid line with squares in blue), respectively. The red shaded area in the middle of the dot-crossed lines and the blue shaded area in the middle of the dotted lines represent the band gap regions in the fully austenitic and fully martensitic phases, respectively.

QZS resonator at low temperature can be four times as that at high temperature.

It should be noted that the wave propagation along the TC-QZS metamaterial presented in Fig. 7 are two special conditions, that is, the SMA is at fully austenitic and fully martensitic phases, respectively. Under normal circumstances, the metallographic phase of the SMA includes austenitic and martensitic phases simultaneously, and the proportions of these two phases are influenced by the temperature applied to the SMA. To state the fundamental principle of low-frequency band gap tuning by further changing the temperature, Fig. 8 shows the effect of temperature on the wave propagation of the TC-QZS metamaterial beam in detail. The variation in the wave transmittance with both the frequency and temperature under the cooling and heating processes are shown in Fig. 8(a) and Fig. 8(b), respectively. The interior of the black dashed line is the frequency range where the wave is suppressed. The closer the colour of the wave transmittance map is to dark blue, the better the wave suppression is. The arrow shows the direction of temperature change.

When the TC-QZS metamaterial experiences the cooling process, the dark blue area increases from low to high frequency. That is, the band gap frequency of the TC-QZS metamaterial shifts from a low- to a high-frequency range. In fact, the sequential change in the metallographic phase is responsible for the variation of the band gap position with decreasing temperature. As the temperature decreases, the martensitic phase component in the SMA gradually increases, the negative stiffness value decreases, and the resonator stiffness increases accordingly, giving rise to the increased resonant frequency of the TC-QZS resonator. In contrast to the cooling process, the band gap frequency of the TC-QZS metamaterial moves from high-frequency range to low-frequency one when the SMA experiences a heating process. Similar to the cooling process, the underlying cause of the variable band gap frequency is the change in the resonator stiffness caused by the transition from the martensitic phase to the austenitic phase. In summary, adjusting the temperature applied to the SMA is a potential avenue for tuning the low-frequency band gap over a wide range.

3.3. Comparison

Note that the theoretical band structures of the TC-QZS metamaterial beam are obtained under the assumption that the resonator undergoes small-amplitude excitation, the stiffness of the TC-QZS resonator is linear and the metamaterial beam possesses an infinite length. However, in practice, it is impossible to fabricate metamaterials with infinite length. The excitation amplitude of the metamaterial was also uncertain. More importantly, the actual stiffness of the TC-QZS resonator is nonlinear due to the existence of a negative stiffness mechanism. Therefore, verifying the correctness of the theoretical band structure is important for the analysis of the TC-QZS metamaterial.

Fig. 9 shows the comparison of both the bandwidth and centre frequency of the band gap obtained by the dispersion relation (DR) and numerical simulation (GM). Note that the centre frequency of the band gap refers to the maximum inhibition effect of the TC-QZS metamaterial within the band gap region. The red solid line with triangles represents the resonant frequency (RF) of the TC-QZS resonator at different SMA temperatures. The bar graph shows the band gap width. Additionally, only part of the results in the temperature range where the phase transition occurs (descending from M_s to M_f and ascending from A_s to A_f, respectively) are presented in Fig. 9 because the band gap of the TC-QZS metamaterial changes only in the temperature range where the SMA undergoes a phase transition during the cooling (the upper panel) and heating (the lower panel) processes.

As shown in Fig. 9, the centre frequencies of both the theoretical and numerical band gaps predicted by the wave transmittance match well. In the numerical results, the frequency range where the wave transmittance is less than 0 dB is wider than the bandwidths predicted by the dispersion relation. This is the result of the consideration of nonlinear stiffness and damping in numerical results. As can be seen from Fig. 5,

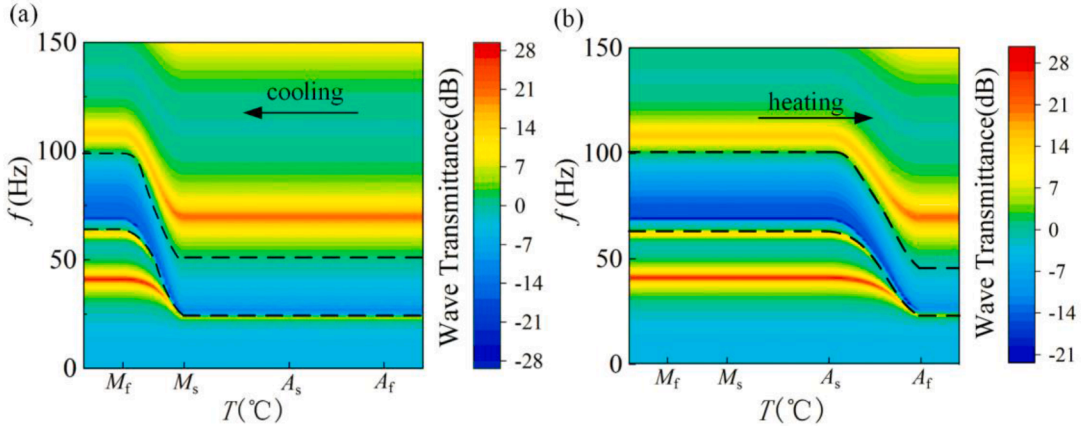

Fig. 8. Wave transmittance of the TC-QZS metamaterial beam influenced by the temperature. The blue area is the part of the wave transmittance which is less than zero, that is, the TC-QZS metamaterial is in the band gap.

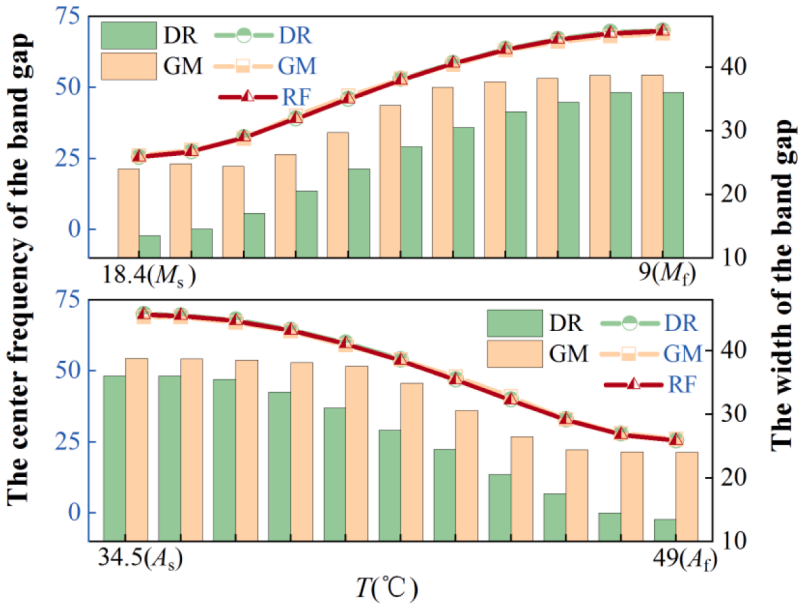

Fig. 9. Comparison of results obtained by dispersion relation (DR) and numerical simulation (GM). The green and orange bars and lines represent the widths and centre frequencies of the band gap obtained by the two methods, respectively. The red line with triangles represents the resonant frequency (RF) of the TC-QZS resonator.

when the mass block vibrates around the equilibrium position, the nonlinear stiffness of the TC-QZS resonator increases with the increase of the relative displacement. As a result, the numerical band gap widens towards high frequencies. At the same time, the consideration of damping in the numerical simulation will also widen the band gap [40,73,74]. Additionally, the resonant frequency of the TC-QZS resonator is in line with the centre frequency revealed by the band structure, which confirms the fundamental principle of the opening of the locally resonant band gap. Therefore, it is feasible to simplify the nonlinear stiffness as a linear stiffness during the cooling process.

4. Discussion

Apart from the SMA temperature, the material, damping ratios and geometrical parameters of the metamaterial affect the band structures, including the frequency, bandwidth, and wave attenuation feature along the metamaterial. To clarify the relationship between the parameters and band structures, the influence of the elastic modulus of the SMA, damping ratio, lattice constant, length and area moment of inertia of the SMA beam in the resonator, and radius of the semi-circular outline on the band gap of the TC-QZS metamaterial are investigated. At the same time, since the temperature of each resonator may be different in practical applications, the band gap structure of the TC-QZS metamaterial with temperature differences is also discussed in this section.

SMAs are typically metal alloys primarily composed of Nickel and Titanium. As the ratio of Nickel or Titanium changes, the material properties of the SMA also change. To determine the influence of the SMA material component on the band structure, Fig. 10(a) shows the wave transmittances of the two types of SMAs in their extreme metallographic phases, which are fully martensitic (blue lines with triangles) and fully austenitic phases (red lines with circles). The solid lines show the wave transmittance corresponding to the SMA used in this study,

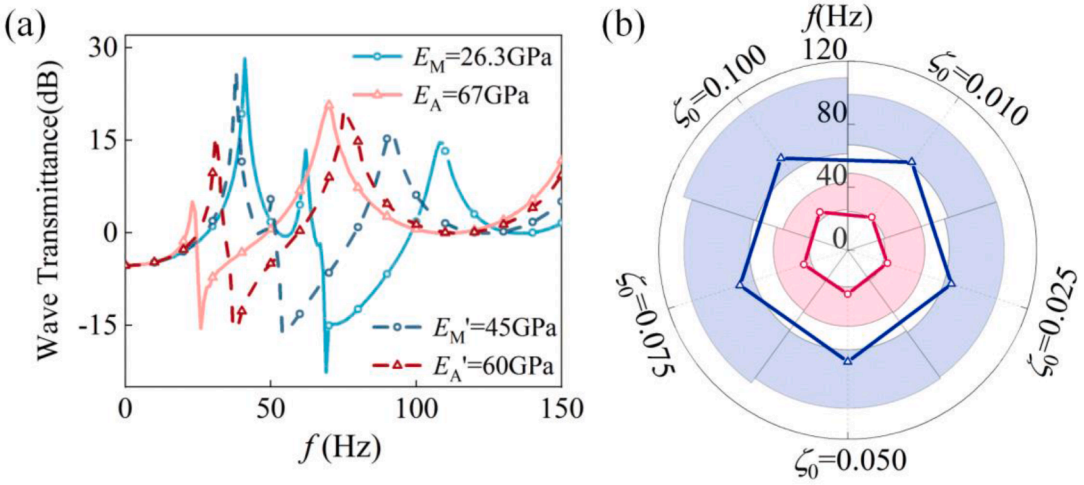

Fig. 10. (a) Change of the wave transmittances caused by different material properties of the SMA. The different ratios of Nickel or Titanium in the SMA will lead to change of the material properties, resulting in different wave transmittances. (b) Changes of the band gap range and centre frequency caused by different the damping ratios of the resonator. Different assembly and lubrication methods influence the damping ratio of the resonator, leading to the variation of the band gap of the metamaterial.

whereas the dashed lines show the wave transmittance realised by the SMA from the reference [65]. The martensitic and austenitic moduli of these two types of SMA are different. It is evident from the figure that the wave transmittance of the TC-QZS metamaterial varies significantly with the elastic modulus. When the elastic modulus of the SMA increases because of the variation in its material components, the band gap shifts from high- to low-frequency range. As a result, replacing the SMA type provides an alternative way to obtain a desired band structure and realise band tuning under the limitation of the resonator geometrical configuration.

Since the SMA is assumed to be always in the state of low stress in this study, the pseudo-elastic effect of the SMA on damping is not considered. However, mechanical friction between components in TC-QZS metamaterial beams can affect the damping ratio. Consequently, the influence of the damping ratio of resonators on the band gap structure of the TC-QZS metamaterial is discussed by changing the damping ratio of the resonator, as shown in Fig. 10(b). In order to observe the limit position of the band gap more intuitively, only the centre frequency of the band gap in the fully martensitic (blue lines with triangles) and fully austenitic (red lines with circles) phases are drawn in this figure. The shaded areas in red and blue show the low-frequency band gap in the fully austenitic phase and the high-frequency band gap in the fully martensitic phase, respectively. As can be seen from the figure, the change of damping ratio has almost no effect on the centre frequency of the band gap, but has a significant influence on the width of the band gap. As the damping ratio increases, the low frequency band gap gradually decreases. This is because the low-frequency resonance is suppressed by damping, which affects the transmittance of the TC-QZS metamaterial. However, in the higher frequency range, an increase in damping will also suppress the vibration of the beam itself, so the frequency range of wave propagation on the beam is widened.

The influences of the other geometric parameters of the SMA beam on the wave transmittance of the TC-QZS metamaterial are shown in Fig. 11. The band gap structures of the TC-QZS metamaterial with different lattice constants are shown in Fig. 11(a). It should be noted that the number of resonators mounted on the TC-QZS metamaterial increases with the decrease of the lattice constant because the length of the substrate beam remains unchanged. With a decrease of the lattice constant, the width of the band gap becomes wider, while the position of the band gap remains unchanged. However, the lattice constant should not be decreased blindly in order to widen the band gap. The selection of the lattice constant should also consider the size of the resonator, the proportional relationship between the mass of the resonator and the substrate beam, and the bearing capacity of the substrate beam. Additionally, the invariance of the band gap frequency when the lattice constant decreases or the number of resonators increases confirms the formation mechanism of the locally resonant band gap. That is, the resonant frequency of the resonator is the sole factor that influences the position of the locally resonant band gap.

Fig. 11(b) delineate the dependence of the length of the SMS beam on the wave transmittance, where the red and green shaded areas represent the band gaps as SMA in the fully austenitic and fully martensitic phases, respectively. The curves with corresponding colour show the change in the centre frequency of the homologous band gap. The band gap of the TC-QZS metamaterial moves to the high-frequency range as the length of the SMA beam increases due to the variation in the resonator stiffness. At the same time, the adjustment range of the band gap controlled by temperature becomes narrow. Specifically, the value of the negative

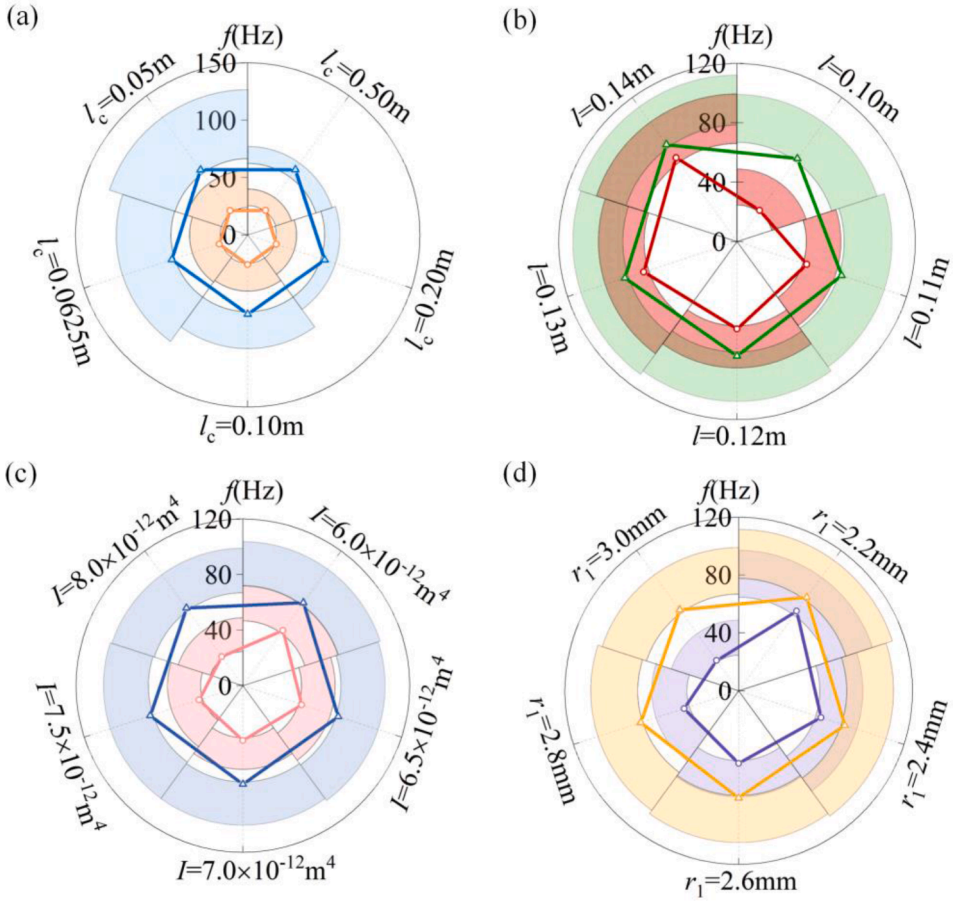

Fig. 11. Changes of the band gap range and centre frequency caused by (a) lattice constant of the TC-QZS metamaterial; (b) length of the SMA beam; (c) area moment of inertia of the SMA beam; (d) radius of the semi-circular outline.

stiffness decreases with an increase in the length of the SMA beam, leading to an increase of the remaining stiffness of the TC-QZS resonator. Because of the intrinsic tie between the resonator stiffness and resonant frequency of the TC-QZS resonator, the variation in the length of the SMA beam induces a change in the resonant frequency and eventually in the centre frequency of the band gap. When the proportion of austenitic phase in SMA increases, that is, the greater the value of the elastic modulus, the influence of the SMA beam length on the negative stiffness is. Therefore, the same length change has a greater influence in the low frequency range.

Fig. 11(c) shows the influence of the area moment of inertia of the SMA beam on the wave transmittance of the TC-QZS metamaterial. The band gap of the TC-QZS metamaterial predicted by the numerical wave transmittance moved to a low frequency as the area moment of inertia of the beam gradually increased and the regulation range of the band gap became larger. This can also be attributed to the variation in remaining stiffness of the resonator caused by the change of the area moment of inertia.

In addition to the geometrical parameters of the SMA, the influence of the structural parameters of the TC-QZS resonator on the wave transmittance is illustrated in Fig. 11. Specifically, with an increase in the radius of the semi-circular, as shown in Fig. 11(d), the band gap of the TC-QZS metamaterial shifts from the high-frequency region to the low-frequency one, and the tunable range of the band gap becomes larger. The underlying cause for such a variation in the band gap lies in the influence of the structural parameters on the stiffness of the TC-QZS resonator. As illustrated in Fig. 2, the mid-span deflection of the SMA beam increases with an increase in the radii of the semi-circular outline and roller or a decrease in the distance between them. Then, the augmentation of the deflection of the beam affects the variation of the resonator stiffness and the resultant downward shift of the band gap.

In the above numerical simulation process, it is assumed that the TC-QZS metamaterial is in an environment of uniform temperature, that is, the SMAs on all resonators are in the same metallic phase state. However, in practical application, the temperatures of different resonators might be difficult to be exactly the same. Fig. 12 then shows the variation of the band gap structure of the TC-QZS metamaterial when the temperature differences between resonators exist. For easy observation, two initial temperatures are assumed to be A_f and M_f, the temperature of each adjacent resonator decreases or increases respectively with a temperature difference of 0.2 °Celsius. The solid yellow lines with the circles in the figures are the transmittances of the TC-QZS metamaterial at the constant temperature A_f or M_f, and the yellow shadow in the upper part of the figure represents the corresponding band gap. The dashed blue lines with triangles are the transmittances of the TC-QZS metamaterial under different temperature states, and the corresponding band gap is the blue shadow in the lower part of the figure. The change of resonator stiffness caused by temperature difference widens the band gap slightly [75], which also provides a new idea for further using of the temperature control mechanism to optimise the band gap structure of TC-QZS.

5. Conclusions

In this study, a temperature-controlled quasi-zero-stiffness (TC-QZS) metamaterial resonator is proposed to achieve low-frequency band gap tuning over a wide frequency range. The proposed TC-QZS resonator is firstly devised through the combination of vertical springs and a negative stiffness mechanism consisting of SMA and a nonlinear geometrical mechanism. Then, a TC-QZS metamaterial beam is proposed by periodically mounting the TC-QZS resonators onto a substrate beam. The effect of the SMA temperature on the stiffness of the TC-QZS resonator is elucidated with the help of a metallic phase transition mechanism. The band structures of the TC-QZS metamaterial are first obtained by deducing the dispersion relation and then verified through numerically predicted wave transmittance. The effectiveness of low-frequency band gap tuning realised by regulating SMA temperature is analysed and assessed. The following conclusions are drawn.

The stiffness of the vertical spring within the TC-QZS resonator can be effectively neutralised by the negative-stiffness mechanism. More importantly, the degree of neutralisation of the stiffness can be easily tuned over a wide range owing to the metallic phase transition of the SMA and the resultant variation in its elastic modulus.

The TC-QZS metamaterial beam can open a band gap in the low-, even ultralow-frequency range after the deployment of the negative-stiffness mechanism. The band structure of the TC-QZS metamaterial beam can be further tuned by changing its material/geometrical parameters and can be widen by introducing temperature differences between resonators.

The TC-QZS metamaterial allows for the band gap tuning in the quadruple numerical range of the centre frequency of band gap and provides a promising approach for tuning the low-frequency band gap over a large frequency range, typically of 25.2–98.5 Hz in the present configuration. Such exceptional tunability of the low-frequency band gap holds great promise for wave manipulation when a large frequency range needs to be accommodated.

The present design of the TC-QZS metamaterial ideally be confined to applications where the substrate beam has no static deformation after assembling the resonator. Future work will focus on redesigning the installation mode of the TC-QZS resonators, establishing a new metamaterial beam model to avoid the influence of mass ratio on the static deformation of substrate beams, and carrying out experimental studies to confirm its effectiveness.

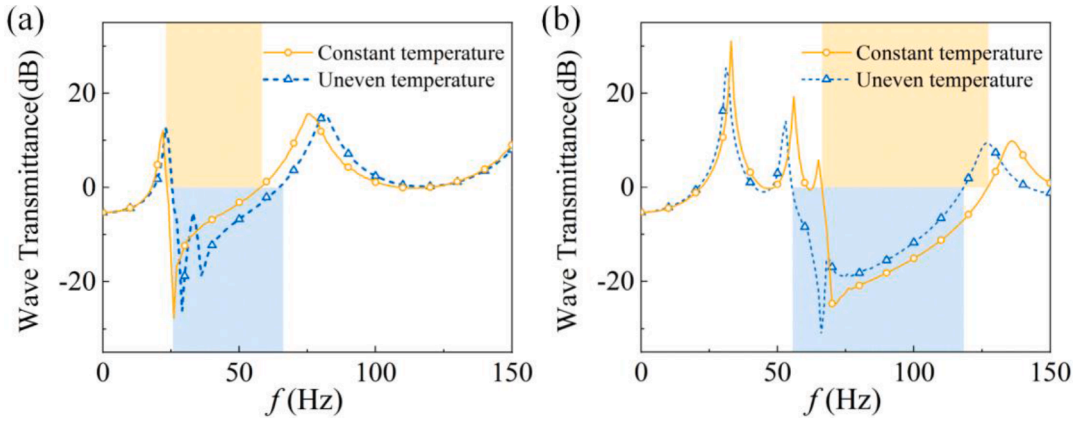

Fig. 12. The influence of the temperature difference between resonators on band gap structure of the TC-QZS metamaterial. (a) High temperature condition, where the constant temperature is A_f. (B) Low temperature condition, where the constant temperature is M_f.

CRediT authorship contribution statement

Zeyi Li: Conceptualization, Methodology, Software, Investigation. **Kai Wang:** Conceptualization, Methodology, Writing – original draft, Funding acquisition. **Tingting Chen:** Data curation, Formal analysis. **Li Cheng:** Methodology, Investigation, Writing – review & editing. **Daolin Xu:** Writing – review & editing. **Jiaxi Zhou:** Writing – review & editing, Funding acquisition.

Declaration of Competing Interest

The authors declare that they have no known competing financial interests or personal relationships that could have appeared to influence the work reported in this paper.

Data availability

Data will be made available on request.

Acknowledgments

This research work was supported by the National Natural Science Foundation of China (Grant Nos. 12272129, 12002122 and 12122206), Natural Science Foundation of Hunan Province (Grant Nos. 2021JJ40092) and the Hong Kong Scholars Program (Grant No. XJ2022012).

References

[1] Martínez-Sala R, Sancho J, Sánchez JV, Gómez V, Llinares J, Meseguer F. Sound attenuation by sculpture. Nature 1995;378:241.
[2] Page JH, Sukhovich A, Yang S, Cowan ML, Van Der Biest F, Tourin A, Fink M, Liu Z, Chan CT, Sheng P. Phononic crystals. Phys Status Solidi Basic Res 2004;241:3454–62.
[3] Askari M, Hutchins DA, Thomas PJ, Astolfi L, Watson RL, Abdi M, Ricci M, Laureti S, Nie L, Freear S. Additive manufacturing of metamaterials: a review. Addit Manuf 2020;36:101562.
[4] Li F-L, Wang Y-S, Zhang C. A BEM for band structure and elastic wave transmission analysis of 2D phononic crystals with different interface conditions. Int J Mech Sci 2018;144:110–7.
[5] Jia Z, Chen Y, Yang H, Wang L. Designing phononic crystals with wide and robust band gaps. Phys Rev Appl 2018;9:44021.
[6] Zhou J, Xiao Q, Xu D, Ouyang H, Li Y. A novel quasi-zero-stiffness strut and its applications in six-degree-of-freedom vibration isolation platform. J Sound Vib 2017;394:59–74.
[7] Nair S, Jokar M, Semperlotti F. Nonlocal acoustic black hole meta structures: achieving broadband and low frequency passive vibration attenuation. Mech Syst Signal Process 2022;169:108716.
[8] Jian W, Xiao-Chun B, Yong X, Ming-Xin G, Dian-Long Y, Ji-Hong W. Low frequency band gaps and vibration reduction properties of a multi-frequency locally resonant phononic plate. Acta Phys Sin 2016;65.
[9] Liu Z, Zhang X, Mao Y, Zhu YY, Yang Z, Chan CT, Sheng P. Locally resonant sonic materials. Science (80-.) 2000;289:1734–6.
[10] Li Z, Hu H, Wang X. A new two-dimensional elastic metamaterial system with multiple local resonances. Int J Mech Sci 2018;149:273–84.
[11] Yu D, Liu Y, Wang G, Zhao H, Qiu J. Flexural vibration band gaps in Timoshenko beams with locally resonant structures. J Appl Phys 2006;100:124901.
[12] Lazarov BS, Jensen JS. Low-frequency band gaps in chains with attached non-linear oscillators. Int J Non Linear Mech 2007;42:1186–93.
[13] Xiao Y, Wen J, Wen X. Flexural wave band gaps in locally resonant thin plates with periodically attached spring–mass resonators. J Phys D Appl Phys 2012;45:195401.
[14] Hussein MI, Leamy MJ, Ruzzene M. Dynamics of phononic materials and structures: historical origins, recent progress, and future outlook. Appl Mech Rev 2014;66.
[15] Wang K, Zhou J, Tan D, Li Z, Lin Q, Xu D. A brief review of metamaterials for opening low-frequency band gaps. Appl Math Mech 2022;43:1125–44.
[16] Hao Z, Cao Q, Wiercigroch M. Nonlinear dynamics of the quasi-zero-stiffness SD oscillator based upon the local and global bifurcation analyses. Nonlinear Dyn 2017;87:987–1014.
[17] Zhou J, Wang K, Xu D, Ouyang H. Local resonator with high-static-low-dynamic stiffness for lowering band gaps of flexural wave in beams. J Appl Phys 2017;121:44902.
[18] Zhou J, Wang K, Xu D, Ouyang H. Multi-low-frequency flexural wave attenuation in Euler–Bernoulli beams using local resonators containing negative-stiffness mechanisms. Phys Lett A 2017;381:3141–8.
[19] Zhou J, Dou L, Wang K, Xu D, Ouyang H. A nonlinear resonator with inertial amplification for very low-frequency flexural wave attenuations in beams. Nonlinear Dyn 2019;96:647–65.
[20] Xie B, Sheng M. Ultralow-frequency band gap in a quasi-zero-stiffness multi-resonator periodic hybrid structure. Wave Motion 2021;107:102825.
[21] He F, Shi Z, Qian D, Tu J, Chen M. Flexural wave bandgap properties in metamaterial dual-beam structure. Phys Lett A 2022:127950.
[22] Hao Z, Cao Q, Wiercigroch M. Two-sided damping constraint control strategy for high-performance vibration isolation and end-stop impact protection. Nonlinear Dyn 2016;86:2129–44.
[23] Wang Q, Zhou J, Wang K, Gao J, Lin Q, Chang Y, Xu D, Wen G. Dual-function quasi-zero-stiffness dynamic vibration absorber: low-frequency vibration mitigation and energy harvesting. Appl Math Model 2023;116:636–54.
[24] Ye T, Nguyen V, Li S. Enhancing the vibratory roller's ride comfort with semi-active seat suspension embedded by quasi-zero stiffness structure. Int J Dyn Control 2023.
[25] Zeng R, Yin S, Wen G, Zhou J. A non-smooth quasi-zero-stiffness isolator with displacement constraints. Int J Mech Sci 2022;225:107351.
[26] Zhao F, Ji J, Ye K, Luo Q. An innovative quasi-zero stiffness isolator with three pairs of oblique springs. Int J Mech Sci 2021;192:106093.
[27] Zhao F, Ji JC, Ye K, Luo Q. Increase of quasi-zero stiffness region using two pairs of oblique springs. Mech Syst Signal Process 2020;144.
[28] Wu Z, Liu W, Li F, Zhang C. Band-gap property of a novel elastic metamaterial beam with X-shaped local resonators. Mech Syst Signal Process 2019;134:106357.
[29] Li ZC, Hao YX, Zhang W, Qiang CX, Li H. Locally resonant bandgap and dynamic responses of meta-sandwich-like plate with L-shaped beam–mass resonators. Int J Dyn Control 2023.
[30] Wang K, Zhou J, Cai C, Xu D, Xia S, Wen G. Bidirectional deep-subwavelength band gap induced by negative stiffness. J Sound Vib 2021;515:116474.
[31] Wang K, Zhou J, Xu D, Ouyang H. Tunable low-frequency torsional-wave band gaps in a meta-shaft. J Phys D Appl Phys 2018;52:55104.
[32] Ye K, Ji JC, Brown T. Design of a quasi-zero stiffness isolation system for supporting different loads. J Sound Vib 2020;471:115198.
[33] Zuo S, Wang D, Zhang Y, Luo Q. Design and testing of a parabolic cam-roller quasi-zero-stiffness vibration isolator. Int J Mech Sci 2022;220:107146.
[34] Yan B, Yu N, Wang Z, Wu C, Wang S, Zhang W. Lever-type quasi-zero stiffness vibration isolator with magnetic spring. J Sound Vib 2022;527:116865.
[35] Wang K, Zhou J, Wang Q, Ouyang H, Xu D. Low-frequency band gaps in a metamaterial rod by negative-stiffness mechanisms: design and experimental validation. Appl Phys Lett 2019;114:251902.
[36] Wang Q, Zhou J, Wang K, Lin Q, Xu D, Wen G. A compact quasi-zero-stiffness device for vibration suppression and energy harvesting. Int J Mech Sci 2023;250:108284.
[37] Liu C, Zhao R, Yu K, Liao B. In-plane quasi-zero-stiffness vibration isolator using magnetic interaction and cables: theoretical and experimental study. Appl Math Model 2021;96:497–522.
[38] Jiang W, Yin M, Liao Q, Xie L, Yin G. Three-dimensional single-phase elastic metamaterial for low-frequency and broadband vibration mitigation. Int J Mech Sci 2021;190:106023.
[39] Zhou J, Pan H, Cai C, Xu D. Tunable ultralow frequency wave attenuations in one-dimensional quasi-zero-stiffness metamaterial. Int J Mech Mater Des 2021;17:285–300.
[40] Cai C, Zhou J, Wu L, Wang K, Xu D, Ouyang H. Design and numerical validation of quasi-zero-stiffness metamaterials for very low-frequency band gaps. Compos Struct 2020;236:111862.
[41] Lin Q, Zhou J, Pan H, Xu D, Wen G. Numerical and experimental investigations on tunable low-frequency locally resonant metamaterials. Acta Mech Solida Sin 2021;34:612–23.
[42] Lin Q, Zhou J, Wang K, Xu D, Wen G, Wang Q, Cai C. Low-frequency locally resonant band gap of the two-dimensional quasi-zero-stiffness metamaterials. Int J Mech Sci 2022;222:107230.
[43] Wang S, Wang M, Guo Z. Adjustable low-frequency bandgap of flexural wave in an Euler-Bernoulli meta-beam with inertial amplified resonators. Phys Lett A. 2021;417:127671.
[44] Wang Z, Zhang Q, Zhang K, Hu G. Tunable digital metamaterial for broadband vibration isolation at low frequency. Adv Mater 2016;28:9857–61.
[45] Miniaci M, Mazzotti M, Amendola A, Fraternali F. Effect of prestress on phononic band gaps induced by inertial amplification. Int J Solids Struct 2021;216:156–66.
[46] Wu L, Wang Y, Zhai Z, Yang Y, Krishnaraju D, Lu J, Wu F, Wang Q, Jiang H. Mechanical metamaterials for full-band mechanical wave shielding. Appl Mater Today 2020;20:100671.
[47] Huang Y, Li J, Chen W, Bao R. Tunable bandgaps in soft phononic plates with spring-mass-like resonators. Int J Mech Sci 2019;151:300–13.
[48] Ning S, Yang F, Luo C, Liu Z, Zhuang Z. Low-frequency tunable locally resonant band gaps in acoustic metamaterials through large deformation. Extrem Mech Lett 2020;35:100623.
[49] Yoo J, Park N-C. Bandgap analysis of a tunable elastic-metamaterial-based vibration absorber with electromagnetic stiffness. Microsyst Technol 2020;26:3339–48.
[50] Yi K, Matten G, Ouisse M, Sadoulet-Reboul E, Collet M, Chevallier G. Programmable metamaterials with digital synthetic impedance circuits for vibration control. Smart Mater Struct 2020;29:35005.
[51] Ren T, Liu C, Li F, Zhang C. Active tunability of band gaps for a novel elastic metamaterial plate. Acta Mech 2020;231:4035–53.

[52] Zhou W, Chen W, Chen Z, Lim C. Actively controllable flexural wave band gaps in beam-type acoustic metamaterials with shunted piezoelectric patches. Eur J Mech 2019;77:103807.
[53] Sugino C, Ruzzene M, Erturk A. Design and analysis of piezoelectric metamaterial beams with synthetic impedance shunt circuits. IEEE/ASME Trans Mechatronics 2018;23:2144–55.
[54] Hu G, Xu J, Tang L, Lan C, Das R. Tunable metamaterial beam using negative capacitor for local resonators coupling. J Intell Mater Syst Struct 2020;31:389–407.
[55] Wang Y, Yang J, Chen Z, Gong X, Du H, Zhang S, Li W, Sun S. Investigation of a novel MRE metamaterial sandwich beam with real-time tunable band gap characteristics. J Sound Vib 2022;527:116870.
[56] Xu J, Lu H, Qin W, Wang P, Bian J. Mechanical shunt resonators-based piezoelectric metamaterial for elastic wave attenuation. Materials (Basel) 2022;15:891.
[57] Wang K, Zhou J, Ouyang H, Cheng L, Xu D. A semi-active metamaterial beam with electromagnetic quasi-zero-stiffness resonators for ultralow-frequency band gap tuning. Int J Mech Sci 2020;176:105548.
[58] Callanan J, Willey CL, Chen VW, Liu J, Nouh M, Juhl AT. Uncovering low frequency band gaps in electrically resonant metamaterials through tuned dissipation and negative impedance conversion. Smart Mater Struct 2022;31:015002.
[59] Chang Y, Zhou J, Wang K, Xu D. Theoretical and experimental investigations on semi-active quasi-zero-stiffness dynamic vibration absorber. Int J Mech Sci 2022;214:106892.
[60] Tan X, Chen S, Wang B, Tang J, Wang L, Zhu S, Yao K, Xu P. Real-time tunable negative stiffness mechanical metamaterial. Extrem Mech Lett 2020;41:100990.
[61] Ning S, Yan Z, Chu D, Jiang H, Liu Z, Zhuang Z. Ultralow-frequency tunable acoustic metamaterials through tuning gauge pressure and gas temperature. Extrem Mech Lett 2021;44:101218.
[62] Brinson LC. One-dimensional constitutive behavior of shape memory alloys: thermomechanical derivation with non-constant material functions and redefined martensite internal variable. J Intell Mater Syst Struct 1993;4:229–42.
[63] Xu MB, Song G. Adaptive control of vibration wave propagation in cylindrical shells using SMA wall joint. J Sound Vib 2004;278:307–26.
[64] Liang C, Rogers CA. A multi-dimensional constitutive model for shape memory alloys. J Eng Math 1992;26:429–43.
[65] Candido de Sousa V, Tan D, De Marqui Jr C, Erturk A. Tunable metamaterial beam with shape memory alloy resonators: theory and experiment. Appl Phys Lett 2018;113:143502.
[66] Candido de Sousa V, Sugino C, De Marqui Junior C, Erturk A. Adaptive locally resonant metamaterials leveraging shape memory alloys. J Appl Phys 2018;124:64505.
[67] Yuan Y, Li J, Bao R, Chen W. A double-layer metastructured beam with contact-separation switchability. Mech Adv Mater Struct 2022;29:1011–9.
[68] Chuang K-C, Lv X-F, Wang Y-H. A bandgap switchable elastic metamaterial using shape memory alloys. J Appl Phys 2019;125:55101.
[69] Lv XF, Xu SF, Huang ZL, Chuang KC. A shape memory alloy-based tunable phononic crystal beam attached with concentrated masses. Phys Lett A 2020;384:126056.
[70] Zhou X, Sun Y, Yang S, Bian Z. Band gap manipulation on P-wave propagating in functionally graded phononic crystal by periodical thermal field. Int J Mech Sci 2021;212:106817.
[71] Zhao Z, Cui X, Yin Y, Li Y, Li M. Thermal tuning of vibration band gaps in homogenous metamaterial plate. Int J Mech Sci 2022;225:107374.
[72] Li H, Li Y, Li J. Negative stiffness devices for vibration isolation applications: a review. Adv Struct Eng 2020;23:1739–55.
[73] Hu X, Zhou C. The effect of various damping on the isolation performance of quasi-zero-stiffness system. Mech Syst Signal Process 2022;171:108944.
[74] Cai C, Zhou J, Wang K, Pan H, Tan D, Xu D, Wen G. Flexural wave attenuation by metamaterial beam with compliant quasi-zero-stiffness resonators. Mech Syst Signal Process 2022;174:109119.
[75] Tian Z, Yu L. Rainbow trapping of ultrasonic guided waves in chirped phononic crystal plates. Sci Rep 2017;7:1–7.